ACSNANO

www.acsnano.org

ARTICLE

Magneto-Optical Detection of Photoinduced Magnetism *via* Chirality-Induced Spin Selectivity in 2D Chiral Hybrid Organic–Inorganic Perovskites

Zhengjie Huang,[▽] Brian P. Bloom,[▽] Xiaojuan Ni, Zheni N. Georgieva, Melissa Marciesky, Eric Vetter, Feng Liu, David H. Waldeck,* and Dali Sun*

Cite This: *ACS Nano* 2020, 14, 10370–10375

Read Online

ACCESS | Metrics & More | Article Recommendations | Supporting Information

ABSTRACT: The recent convergence of chiral molecules with metal halide perovskite frameworks gives rise to an interesting family of chiral systems: two-dimensional, chiral hybrid organic–inorganic perovskites (chiral-HOIPs). While possessing photovoltaic properties of traditional HOIPs, this class of materials is endowed with chirality through its organic ligands in which the degeneracy of the electron spin in charge transport is broken. That is, the chirality-induced spin selectivity (CISS) effect manifests, making it a promising platform to bridge opto-spintronic studies and the CISS effect. In this work, chiral-HOIP/NiFe heterostructures are studied by means of the magneto-optical Kerr effect using a Sagnac interferometer. Upon illumination of the chiral-HOIPs, the Kerr signal at the chiral-HOIP/NiFe interface changes, and a linear dependence of the response on the magnetic field is observed. The sign of the slope was found to depend on the chirality of the HOIPs. The results demonstrate the utility of chiral-HOIP materials for chiral opto-spintronic applications.

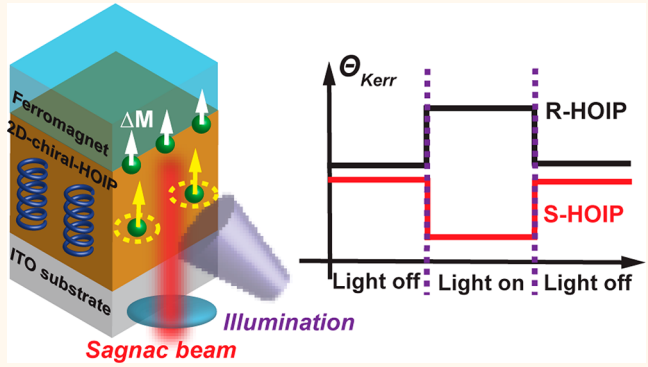

KEYWORDS: *chiral hybrid organic–inorganic perovskites, chirality-induced spin selectivity effect, photoinduced magnetism, magneto-optics, Sagnac interferometer*

The growing field of spintronics research holds promise for a wide array of applications in information technology and quantum computation.[1,2] The central focus of the spintronics field is the generation, manipulation, and detection of spin-encoded information. For example, in a spin valve, one of the most important inventions in the spintronics field, spin current is generated through the spin-selective transport of magnetized ferromagnetic electrodes.[3] Recently, the chiral-induced spin selectivity (CISS) effect[4−6] has been used to demonstrate device strategies that manipulate the electron spin quantum number for spintronic applications.[7−10] Spin-selective transport has been observed for a variety of proteins, chiral molecules and their assemblies, oligopeptides, double-stranded DNA, and inorganic semiconductors. Additionally, studies have shown that the electronic coupling between chiral molecules and ferromagnetic interfaces manifest a "spinterface" effect,[11] similar to those found in traditional achiral organic-ferromagnetic interfaces: induced magnetization[12−14] and manipulation of spin-to-charge conversion,[15] but they display a dependence on the enantiomeric form of the molecule.

This work examines the opto-spintronic response of chiral two-dimensional hybrid organic–inorganic perovskite (chiral-HOIP) films in relation to the CISS effect. Previous studies have shown the promise of achiral-HOIPs for opto-spintronic applications owing to their large tunable spin–orbit couplings and spin-dependent optical selection rules.[16,17] The recent advances for imparting chirality onto perovskite nanostructures[18−22] gives rise to a class of materials that possesses chiro-

Received: May 13, 2020
Accepted: July 17, 2020
Published: July 17, 2020

https://dx.doi.org/10.1021/acsnano.0c04017
ACS Nano 2020, 14, 10370–10375

optical activity as well as the photovoltaic properties traditionally present in HOIPs. Furthermore, magnetic conductive probe atomic force microscopy and magneto-resistance measurements show that chiral-HOIP films exhibit spin filtering capabilities consistent with the predicted CISS effect.[23]

Here, the magnetic field effects of chiral-HOIPs interfaced with NiFe contacts are studied using the magneto-optic Kerr effect (MOKE). This technique was chosen because of its proven sensitivity to small amounts of spin accumulation.[24,25] Figure 1 outlines the general scheme of the experiment. A 405 nm laser photoexcites the chiral-HOIP, and a Sagnac interferometer is used to probe the change in out-of-plane magnetization using a 1550 nm laser beam that is incident on the sample's surface along its normal direction. As a result of the chiral-HOIP's optoelectronic response and the CISS effect, a spin-polarized photocurrent should manifest and introduce an effective net magnetization to the top NiFe layer at the interface (Figure 1). This all-optical excitation and measurement scheme demonstrates an alternative approach for studying the CISS effect which is not prone to artifacts from charging and shorting that can occur in electrical transport measurements.

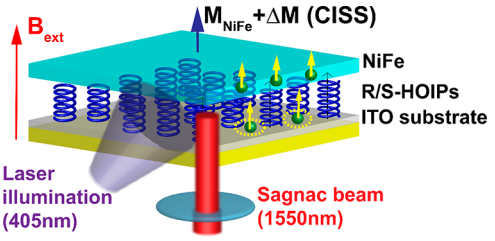

Figure 1. A sketch of a generalized scheme describing the Sagnac MOKE experiment for the light-driven CISS-induced interfacial magnetization at the interface of *R*/*S*-chiral-HOIP and NiFe substrate. The HOIP is illuminated by a 405 nm laser through the ITO substrate. The resulting extra out-of-plane magnetization (Δ*M*(CISS)) at the chiral-HOIP/NiFe interface is measured by the Sagnac MOKE approach. The blue springs represent the HOIPs, and the green dots represent the spin-polarized photogenerated carriers (yellow arrows) under the illumination.

RESULTS AND DISCUSSION

The synthesis of chiral-HOIPs was performed following previously published protocols[26] and then spin-coated onto precleaned indium tin oxide (ITO) substrates. The chiral perovskite comprises 1-phenylethylamonium lead iodide ($(C_8H_{11}N)_2PbI_4$). The scheme in Figure 2a depicts the layered structure of the HOIP and illustrates how the chiral *S*- or *R*-phenylethylamine (*S*/*R*-PEA) ligands separate the lead halide octahedral layers. Figure 2b shows representative circular dichroism spectra of the HOIPs using *S*- (green, *S*-HOIP)/*R*-phenylethylamine (purple, *R*-HOIP) films, which exhibit an approximate mirror image symmetry. After the *R*/*S*-HOIP film formation, 15 nm of ferromagnetic NiFe was evaporated using e-beam deposition on top of the chiral-HOIP layer (see Methods).

The prepared sample was placed in an electromagnet, and the magnetic field was applied along the out-of-plane direction (Figure S1). The sample area was illuminated through the transparent ITO substrate by 405 nm light from a diode laser. The sample was illuminated at a low laser intensity (≤0.6 mW) to suppress laser-induced heating. The Kerr signal was collected by the Sagnac probing beam (1550 nm) through the backside of the sample and overlapping with the 405 nm illumination area at the HOIP/NiFe interface. Because the chiral-HOIP layer has no absorbance at 1550 nm, this experimental design enables direct measurement of the magnetic response at the chiral-HOIP/NiFe interface without perturbing the system. It is anticipated that the out-of-plane net magnetization response stemming from the CISS effect

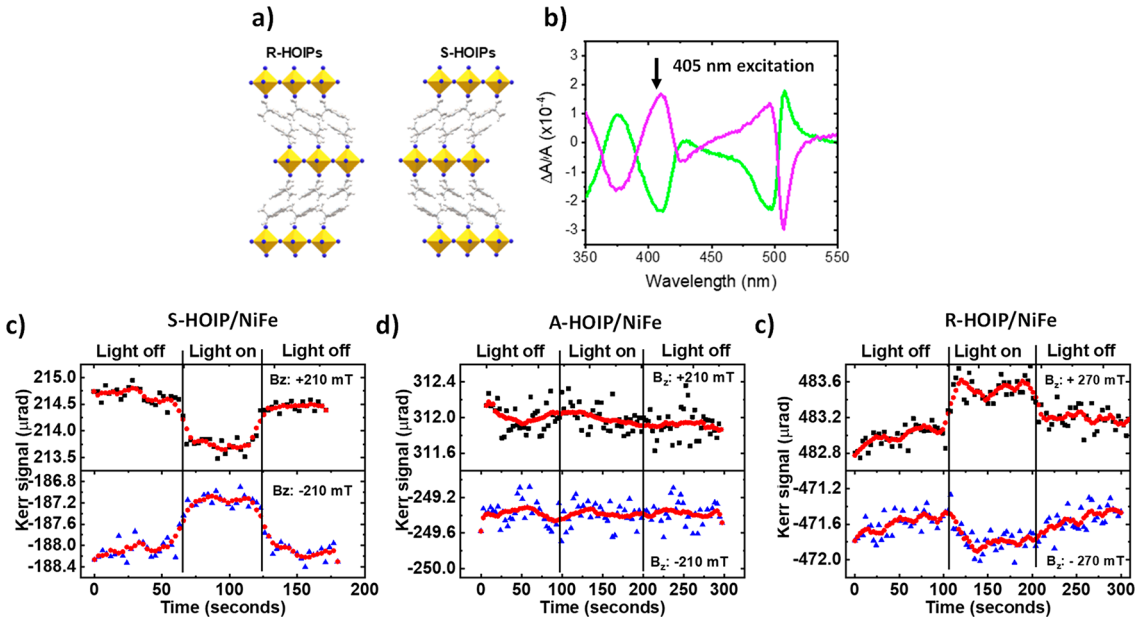

Figure 2. (a) A cartoon illustrating the chiral structure of the *S*- (left) and *R*-HOIPs (right). (b) The measured CD spectra for *S*-HOIP (green) and *R*-HOIP (purple) thin films. (c−e) The change in Kerr signal upon photoexcitation for samples with *S*-HOIP/NiFe, A-HOIP/NiFe, and *R*-HOIP/NiFe under positive (top, black) and negative (bottom, blue) out-of-plane external magnetic field, respectively. The red line is an adjacent average smoothing of the data.

https://dx.doi.org/10.1021/acsnano.0c04017
ACS Nano 2020, 14, 10370−10375

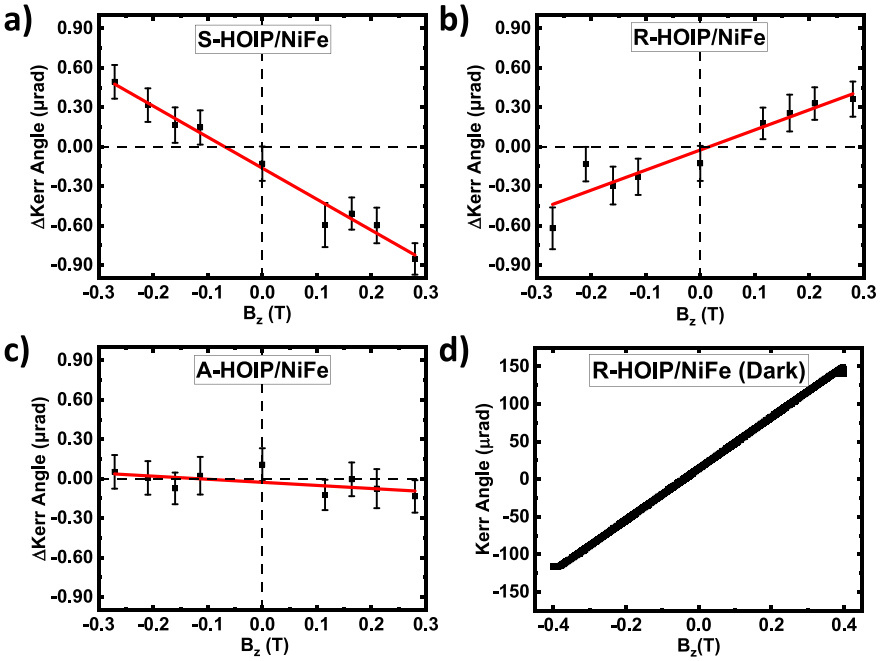

Figure 3. Photoinduced change in the Kerr angle (black, squares) is plotted as a function of external magnetic field. (a−c) Correspond to *S*-HOIP/NiFe, *R*-HOIP/NiFe, and *A*-HOIP/NiFe, respectively. The red line is a linear fit to the data. The Kerr signals have been averaged by four cycles of the illumination to improve the signal-to-noise. (d) Out-of-plane overall *M*−*H* loop for the *R*-HOIP/NiFe sample measured by Sagnac MOKE without the illumination. Note that a 1.0 μrad change in the Kerr angle corresponds to ∼3 mT.

coincides with the polar MOKE configuration, which has the highest Kerr sensitivity (Figure S1). The laser power of the probing Sagnac beam was kept <20 μW to prevent potential laser-induced heating.[25] Changes in the Kerr response under the laser illumination were recorded as a function of time. Comparison of the response under 405 nm illumination to the response in the dark was used to separate the photoresponse from the total magnetization of the NiFe film and the background drift.

Figure 2c−e shows the time evolution of the Kerr angle and how it changes under 405 nm illumination for different external magnetic field directions and for three different sample types: *S*-HOIPs/NiFe (Figure 2c), A-HOIPs/NiFe (Figure 2d), and *R*-HOIP/NiFe (Figure 2e). The data reveal that the photoinduced Kerr response is sensitive to both the chirality of the HOIPs and the external magnetic field. At B_z = +210 mT, the *S*- HOIPs (Figure 2c, top) exhibit a decrease in Kerr signal upon photoexcitation on the order of a microradian ($\Delta\theta_{Kerr} \approx -0.8$ μrad), whereas the *R*-HOIP/NiFe (Figure 2e, top) displays an increase in Kerr signal upon photoexcitation. When the external magnetic field is reversed, an opposite change of Kerr signal is observed in both samples. In contrast to the chiral-HOIP/NiFe samples, the same experiment has been performed on achiral-HOIP/NiFe samples, using 2-phenylethylamine ligands (A-HOIPs). The achiral sample does not exhibit any significant change in Kerr signal upon photoexcitation (Figure 2d). These data suggest that photoexcitation generates a magnetization at the NiFe surface (*i.e.*, the extra Kerr signal), which adds to the magnetization of the NiFe film, and that the sign of the spin-polarization depends on the chirality of the chiral-HOIPs, thus implying that the photocurrent generated in the chiral films must be spin-polarized.

Figure 3a−c shows the magnetic field dependence of the photoinduced Kerr signal for *S*-HOIP/NiFe, *R*-HOIP/NiFe, and A-HOIP/NiFe samples, respectively. The change in Kerr angle exhibits a linear dependence on the external magnetic field, showing no saturation up to 0.3 T. The *S*-HOIP/NiFe (Figure 3a) gives a slope of −2.36 μrad/T with an error of ±0.11 μrad/T. The *R*-HOIP/NiFe (Figure 3b) shows a slope of +1.53 μrad/T with an error of ±0.20 μrad/T. The fitting errors here are mainly determined by the Sagnac sensitivity and sample stability under the light illumination as shown in Figure 2. The A-HOIP/NiFe gives a best fit slope of −0.23 μrad/T which is roughly within the error of ±0.13 μrad/T, indicating no significant response over this magnetic field range. Thus, the photogenerated magnetic response changes significantly with the external magnetic field for the chiral samples and has opposite signs for the two enantiomers (*R*-HOIP and *S*-HOIP). Conversely, the A-HOIP does not display a significant photoresponse or applied field dependence.

By scaling the MOKE signal $\Delta\theta_{Kerr}$ for the *R*-HOIP/NiFe in the dark to its known magnetization, it is possible to estimate the size of the photogenerated magnetization from the photogenerated change in $\Delta\theta_{Kerr}$. The Kerr signal of the *R*-HOIP/NiFe sample in the dark is ∼150 μrad (see Figure 3d), whereas the photoinduced $\Delta\theta_{Kerr}$ is ∼1 μrad, so that the effective photogenerated magnetization, Δ*M*, is about 0.7% of the total observed magnetization. This comparison indicates that an effective out-of-plane magnetic field of ∼ ±2 mT acts on the NiFe layer. Note, while it is believed that Δ*M* is rooted in spin polarization-mediated effects, the percent change in magnetic field does necessitate a similar magnitude of spin polarization. The magnitude of the photoinduced effective field is orders of magnitude lower than that estimated from photoemission measurements at DNA/Au interfaces (up to tens of Tesla),[27] but it is consistent with recent observations of the NiFe/chiral-molecule interface using the anomalous Hall effect.[13] Elucidating the origins of these differences requires further study, however it could arise from limited photogenerated carriers under the low light intensity (<0.6 mW) and

https://dx.doi.org/10.1021/acsnano.0c04017
ACS Nano 2020, 14, 10370−10375

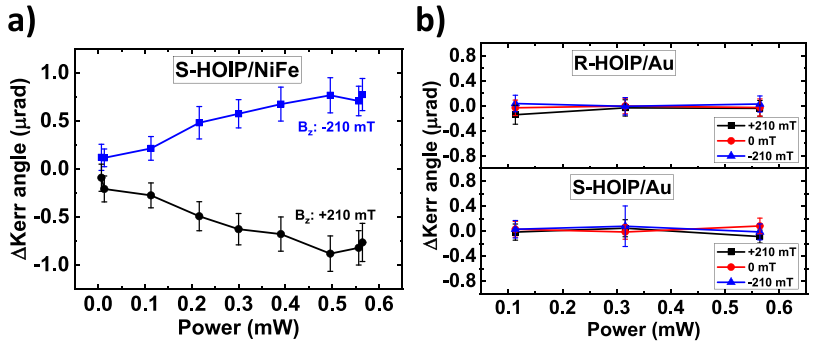

Figure 4. Excitation power dependence studies of the ΔKerr angle. (a) The power dependence for *S*-HOIP/NiFe under +210 mT (black, circles) and −210 mT (blue, squares) external magnetic field. (b) Experiments of architectures in which the NiFe layer is replaced by gold for both *R*- (top) and *S*-HOIP/Au (bottom) with +210 mT (black), 0 mT (red), and −210 mT (blue) external magnetic fields.

differences in spin relaxation rates for the two types of experiments, among others.

The influence of the incident excitation (405 nm) power on the magnitude of the Kerr signal was measured and is shown in Figure 4. Figure 4a shows the change in Kerr angle for samples fabricated with *S*-HOIPs under a positive (black, circles) and negative (blue, squares) magnetic field, respectively. The $\Delta\theta_{Kerr}$ signal in the *S*- HOIP/NiFe sample decreases (increases) when the illumination intensity increases at positive (negative) magnetic fields, until it saturates at ∼0.6 mW. An increase in photon flux generates a larger change in the Kerr angle, presumably arising from more photocurrent density in the HOIP film, and hence results in more exchange current with the ferromagnetic substrate that increases the net magnetization. The saturation at the low light intensity implies an interfacial effect instead of a bulk photocurrent in the thick chiral-HOIPs film (∼300 nm), which is consistent with the spin diffusion length of the generated spin-polarized carriers limited to within 5 nm at room temperature.[28,29]

To further validate that the exchange current between the adjacent ferromagnetic NiFe layer and spin-polarized photocarriers in the chiral-HOIPs gives rise to the extra Kerr signals, control architectures were studied in which the NiFe layer was replaced with Au (Figure 4b). The data shown in Figure 4b for *R*-HOIP/Au (top) and *S*-HOIP/Au (bottom), at applied magnetic fields of +210 mT (black), 0 mT (red), and −210 mT (blue), show no discernible change in Kerr signal upon photoexcitation. To eliminate the possibility of magnetic fields generated by sample heating or direct photoexcitation effects of the ferromagnetic substrate, control experiments were performed in which NiFe was deposited directly onto an ITO substrate; architectures without the presence of chiral-HOIPs. These data are presented in Figures S2 and S3 and show that no substantial change in Kerr angle occurs for these samples. As a further control experiment, the chiral-HOIP/NiFe assemblies were also studied under 808 nm illumination (Figure S4), for which the perovskite absorbance is negligible, and in this case no Kerr response was observed. Thus, the laser heating-related reduction of the bulk magnetization in the NiFe can be excluded, as can the change of the Verdet constant of the chiral-HOIPs.[30] Therefore, the photoinduced Kerr response of the chiral-HOIP/NiFe assemblies requires both the chiral-HOIP and the ferromagnetic layer; namely, the spin-polarized photogenerated carriers in the chiral-HOIP film are needed to "activate" the interfacial magnetization of the adjacent ferromagnet.

We propose that the observed changes in the photoinduced Kerr signal manifest from contributions of two correlated phenomena: (i) a spin-filtering of the photogenerated carriers via the CISS effect and (ii) a hybridization/magnetic proximity effect at the "spinterface" formed between the chiral-HOIP and the ferromagnetic layer. Density functional theory (DFT) calculations have been performed to study the possible magnetic proximity effect between the NiFe substrate and the chiral-HOIPs (see Figures S6−S8). To simplify the calculation, only the "active" components, that is, the chiral molecules which align perpendicularly as those in the HOIP crystal structure, but without adding the PbI_6 inorganic framework, were considered. The configurations of *R*-PEA/NiFe and *S*-PEA/NiFe with the chiral centers of *R*(*S*)-PEA facing the NiFe substrate (lattice constant of 4.997 Å) are shown in Figure S6b,c, respectively. The calculated density of states (DOS) of NiFe, *R*-PEA/NiFe, and *S*-PEA/NiFe (Figure S6d,e), indicate that there is not a significant change of the spin-polarization degree in the DOS in Ni or Fe atoms after the addition of the chiral molecules. The molecular chirality alone is unlikely to cause a change of magnetization of the NiFe substrate directly because of the relatively poor coupling. Therefore, we hypothesize that the inorganic perovskite framework, hybridized with its frontier molecular orbitals and imprinted with the chiral molecules, must be responsible for the observed photoinduced magnetism *via* the CISS effect. It is possible that the CISS effect in chiral-HOIPs not only generates spin-polarized current but also forms "local" magnetic states which may be coupled or mediated by polarons or delocalized carriers that are formed in the metal−halogen framework under photoexcitation.[31,32] A strong inter- or intralayer coupling may result in an effective net magnetization even at room temperature, which changes as a function of external magnetic field as shown in Figure 5. We anticipate that the generation of carriers/polarons is crucial in determining the amplitude of the CISS effect, exchange couplings, and resulting interfacial magnetization, which requires further studies to understand sufficiently.

CONCLUSIONS

This work demonstrates the rich characteristics of chiral-HOIPs for bridging opto-spintronic applications with the CISS effect, that is, chiral opto-spintronics. Magneto-optic Kerr rotation measurements prove that linearly polarized excitation of chiral-HOIPs can change the magnetization of an adjacent ferromagnetic substrate. Demonstration of the existence of interfacial magnetization states *via* the CISS effect in chiral-

https://dx.doi.org/10.1021/acsnano.0c04017
ACS Nano 2020, 14, 10370−10375

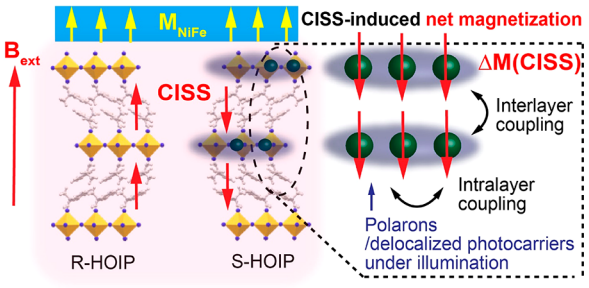

Figure 5. Schematic illustration of the proposed photoinduced magnetism at the NiFe/chiral-HOIP interface. The generation of a net magnetization mediated by spin-dependent polarons/photocarriers *via* the CISS effect is formed in the chiral-HOIPH structure next to the NiFe layer under the illumination.

HOIPs may aid in developing quantitative models for CISS by relaxing the large spin−orbit coupling condition required for the proposed CISS effect. This will shed light on CISS-related behaviors observed in other chiral systems. Moreover, the Sagnac MOKE technique provides a means to directly probe the net magnetization at the molecular level and allows for "benchtop" precise magnetic measurements without large-scale facilities.

METHODS

Chiral-Perovskite Material Synthesis. Chiral-HOIPs were synthesized following previously published protocols.[26] Briefly, 200 mg of PbO was dissolved in 6.0 mL of 57% HI solution and 200 μL of either *R*- or *S*-phenylethylamine was added to the solution. The combination resulted in a precipitate which was dissolved by heating in a silicone oil bath at 100 °C. The reaction was then slowly cooled to room temperature, causing crystallization. The crystallites were collected and washed three times with toluene using a Buchner funnel and then dried in a desiccator for 2 days before use. For the preparation of achiral-HOIPs, an equimolar amount of 2-phenylethylamine was used in place of the *R*- or *S*-phenylethylamine.

Sample Preparation and Sagnac MOKE Measurement. The fabrication of all devices for MOKE measurements was performed using a nitrogen filled glovebox. A 25% by mass solution of the HOIP crystallites was dissolved in DMF, and ∼0.15 μL/mm^2 of solution was drop cast onto a freshly cleaned ITO substrate. The substrate was then spun at 5000 rpm for 30 s and then baked at 100 °C for 8 min. E-beam evaporation was then used to deposit 15 nm of either NiFe or Au onto the substrate at a rate of 0.2 Å/s, followed by a careful encapsulation to prevent the thin film from degrading during the measurement. The prepared sample was placed in an electromagnet (GMW Associates). The Kerr signal was measured in a Faraday configuration (*i.e.*, Polar MOKE configuration) at room temperature. The spot size for the overlapped laser illumination and Sagnac beam is 1 mm and 0.5 mm, respectively. 405 nm is chosen because of the maximum circular dichroism response in *R*- and *S*-HOIP thin films at this wavelength, as shown in Figure 2b. The Kerr signals have been averaged by four cycles of the illumination to improve the signal-to-noise.

DFT Calculation. The first-principles calculations were performed using the Vienna *Ab Initio* Simulation Package based on the projected augmented wave approach within the framework of density functional theory.[33,34] The generalized gradient approximation in the Perdew, Burke, and Ernzerhof form was used for the exchange−correlation functional.[35,36] All the self-consistent calculations were performed with a plane-wave cutoff of 500 eV on a 11 × 11 × 1 Monkhorst−Pack *k*-point mesh. A vacuum layer with a thickness of larger than 15 Å was adopted to ensure the decoupling between the neighboring slabs under the periodic boundary condition. All the structures were fully relaxed until the atomic force was less than 0.01 eV/Å. The molecular properties of *R*(*S*)-PEA were carried out using Gaussian16 with B3LYP functional and 3-21G basis set (Gaussian 16 revision C).

ASSOCIATED CONTENT

Supporting Information

The Supporting Information is available free of charge at https://pubs.acs.org/doi/10.1021/acsnano.0c04017.

Detailed description of the Sagnac microscope and measurement set up; control experiment #1: NiFe only sample under 405 nm illumination; control experiment #2: NiFe only sample under 808 nm illumination; control experiment #3: S-HOIP/NiFe sample under 808 nm illumination; control experiment #4: *R*/*S* and A-HOIP only sample under 405 nm illumination; further discussion and DFT calculations (PDF)

AUTHOR INFORMATION

Corresponding Authors

David H. Waldeck − *Department of Chemistry, University of Pittsburgh, Pittsburgh, Pennsylvania 15260, United States;* orcid.org/0000-0003-2982-0929; Email: dave@pitt.edu

Dali Sun − *Department of Physics and Organic and Carbon Electronics Lab (ORaCEL), North Carolina State University, Raleigh, North Carolina 27695, United States;* orcid.org/0000-0003-4662-3265; Email: dsun4@ncsu.edu

Authors

Zhengjie Huang − *Department of Physics, North Carolina State University, Raleigh, North Carolina 27695, United States*

Brian P. Bloom − *Department of Chemistry, University of Pittsburgh, Pittsburgh, Pennsylvania 15260, United States;* orcid.org/0000-0001-9581-9710

Xiaojuan Ni − *Department of Materials Science and Engineering, University of Utah, Salt Lake City, Utah 84112, United States;* orcid.org/0000-0002-5845-7404

Zheni N. Georgieva − *Department of Chemistry, University of Pittsburgh, Pittsburgh, Pennsylvania 15260, United States;* orcid.org/0000-0001-7091-4965

Melissa Marciesky − *Department of Chemistry, University of Pittsburgh, Pittsburgh, Pennsylvania 15260, United States*

Eric Vetter − *Department of Physics and Department of Materials Science and Engineering, North Carolina State University, Raleigh, North Carolina 27695, United States;* orcid.org/0000-0002-9596-160X

Feng Liu − *Department of Materials Science and Engineering, University of Utah, Salt Lake City, Utah 84112, United States;* orcid.org/0000-0002-3701-8058

Complete contact information is available at: https://pubs.acs.org/10.1021/acsnano.0c04017

Author Contributions

$^{\nabla}$These authors equally contributed to this work.

Notes

The authors declare no competing financial interest.

ACKNOWLEDGMENTS

D.S. acknowledges the support from National Science Foundation ECCS 1936527. Device fabrication is partially supported by National Science Foundation ECCS 1933297. D.H.W. acknowledges the support of the Department of Energy (grant no. ER46430). Work at Utah is supported by US Department of Energy (grant no. DE-FG02-04ER46148). F.L.

acknowledges NERSC and CHPC at the University of Utah for providing the computing resources.

REFERENCES

(1) Wolf, S. A.; Awschalom, D. D.; Buhrman, R. A.; Daughton, J. M.; von Molnár, S.; Roukes, M. L.; Chtchelkanova, A. Y.; Treger, D. M. Spintronics: A Spin-Based Electronics Vision for the Future. *Science* **2001**, *294*, 1488.
(2) Wolf, S. A.; Chtchelkanova, A. Y.; Treger, D. M. Spintronics—A Retrospective and Perspective. *IBM J. Res. Dev.* **2006**, *50*, 101−110.
(3) Bader, S. D.; Parkin, S. S. P. Spintronics. *Annu. Rev. Condens. Matter Phys.* **2010**, *1*, 71−88.
(4) Naaman, R.; Paltiel, Y.; Waldeck, D. H. Chiral Molecules and the Electron Spin. *Nat. Rev. Chem.* **2019**, *3*, 250−260.
(5) Naaman, R.; Waldeck, D. H. Chiral-Induced Spin Selectivity Effect. *J. Phys. Chem. Lett.* **2012**, *3*, 2178−2187.
(6) Naaman, R.; Waldeck, D. H. Spintronics and Chirality: Spin Selectivity in Electron Transport through Chiral Molecules. *Annu. Rev. Phys. Chem.* **2015**, *66*, 263.
(7) Michaeli, K.; Varade, V.; Naaman, R.; Waldeck, D. H. A New Approach towards Spintronics-Spintronics with No Magnets. *J. Phys.: Condens. Matter* **2017**, *29*, 103002.
(8) Koplovitz, G.; Primc, D.; Ben Dor, O.; Yochelis, S.; Rotem, D.; Porath, D.; Paltiel, Y. Magnetic Nanoplatelet-Based Spin Memory Device Operating at Ambient Temperatures. *Adv. Mater.* **2017**, *29*, 1606748.
(9) Dor, O. B.; Yochelis, S.; Mathew, S. P.; Naaman, R.; Paltiel, Y. A Chiral-Based Magnetic Memory Device without a Permanent Magnet. *Nat. Commun.* **2013**, *4*, 2256.
(10) Al-Bustami, H.; Koplovitz, G.; Primc, D.; Yochelis, S.; Capua, E.; Porath, D.; Naaman, R.; Paltiel, Y. Single Nanoparticle Magnetic Spin Memristor. *Small* **2018**, *14*, 1801249.
(11) Sanvito, S. Molecular Spintronics: The Rise of Spinterface Science. *Nat. Phys.* **2010**, *6*, 562−564.
(12) Koplovitz, G.; Leitus, G.; Ghosh, S.; Bloom, B. P.; Yochelis, S.; Rotem, D.; Vischio, F.; Striccoli, M.; Fanizza, E.; Naaman, R.; Waldeck, D. H.; Porath, D.; Paltiel, Y. Single Domain 10 nm Ferromagnetism Imprinted on Superparamagnetic Nanoparticles Using Chiral Molecules. *Small* **2019**, *15*, 1804557.
(13) Ben Dor, O.; Yochelis, S.; Radko, A.; Vankayala, K.; Capua, E.; Capua, A.; Yang, S.-H.; Baczewski, L. T.; Parkin, S. S. P.; Naaman, R.; Paltiel, Y. Magnetization Switching in Ferromagnets by Adsorbed Chiral Molecules without Current or External Magnetic Field. *Nat. Commun.* **2017**, *8*, 14567.
(14) Ben Dor, O.; Morali, N.; Yochelis, S.; Baczewski, L. T.; Paltiel, Y. Local Light-Induced Magnetization Using Nanodots and Chiral Molecules. *Nano Lett.* **2014**, *14*, 6042−6049.
(15) Ghosh, S.; Mishra, S.; Avigad, E.; Bloom, B. P.; Baczewski, L. T.; Yochelis, S.; Paltiel, Y.; Naaman, R.; Waldeck, D. H. Effect of Chiral Molecules on the Electron's Spin Wavefunction at Interfaces. *J. Phys. Chem. Lett.* **2020**, *11*, 1550−1557.
(16) Odenthal, P.; Talmadge, W.; Gundlach, N.; Wang, R.; Zhang, C.; Sun, D.; Yu, Z.-G.; Vardeny, Z. V.; Li, Y. S. Spin-Polarized Exciton Quantum Beating in Hybrid Organic-Inorganic Perovskites. *Nat. Phys.* **2017**, *13*, 894−899.
(17) Zhang, C.; Sun, D.; Sheng, C.-X.; Zhai, Y. X.; Mielczarek, K.; Zakhidov, A.; Vardeny, Z. V. Magnetic Field Effects in Hybrid Perovskite Devices. *Nat. Phys.* **2015**, *11*, 427−434.
(18) Dong, Y.; Zhang, Y.; Li, X.; Feng, Y.; Zhang, H.; Xu, J. Chiral Perovskites: Promising Materials toward Next-Generation Optoelectronics. *Small* **2019**, *15*, 1902237.
(19) Georgieva, Z. N.; Bloom, B. P.; Ghosh, S.; Waldeck, D. H. Imprinting Chirality onto the Electronic States of Colloidal Perovskite Nanoplatelets. *Adv. Mater.* **2018**, *30*, 1800097.
(20) Xiao, L.; An, T.; Wang, L.; Xu, X.; Sun, H. Novel Properties and Applications of Chiral Inorganic Nanostructures. *Nano Today* **2020**, *30*, 100824.
(21) Long, G.; Jiang, C.; Sabatini, R.; Yang, Z.; Wei, M.; Quan, N.; Liang, Q.; Rasmita, A.; Askerka, M.; Walters, G.; Gong, X.; Xing, J.; Wen, X.; Quintero-Bermudez, R.; Yuan, H.; Xing, G.; Wang, X. R.; Song, D.; Voznyy, O.; Zhang, M.; Hoogland, S.; Gao, W.; Xiong, Q.; Sargent, E. H. Spin Control in Reduced-Dimensional Chiral Perovskites. *Nat. Photonics* **2018**, *12*, 528−533.
(22) Long, G.; Zhou, Y.; Zhang, M.; Sabatini, R.; Rasmita, A.; Huang, L.; Lakhwani, G.; Gao, W. Theoretical Prediction of Chiral 3D Hybrid Organic-Inorganic Perovskites. *Adv. Mater.* **2019**, *31*, 1807628.
(23) Lu, H.; Wang, J.; Xiao, C.; Pan, X.; Chen, X.; Brunecky, R.; Berry, J. J.; Zhu, K.; Beard, M. C.; Vardeny, Z. V. Spin-Dependent Charge Transport through 2D Chiral Hybrid Lead-Iodide Perovskites. *Sci. Adv.* **2019**, *5*, No. eaay0571.
(24) Liu, H.; McLaughlin, R.; Sun, D.; Vardeny, Z. V. Long-Range Transverse Spin Seebeck Effect in Permalloy Stripes Using Sagnac Interferometer Microscopy. *J. Phys. D: Appl. Phys.* **2018**, *51*, 134003.
(25) McLaughlin, R.; Sun, D.; Zhang, C.; Groesbeck, M.; Vardeny, Z. V. Optical Detection of Transverse Spin-Seebeck Effect in Permalloy Film Using Sagnac Interferometer Microscopy. *Phys. Rev. B: Condens. Matter Mater. Phys.* **2017**, *95*, 180401.
(26) Ahn, J.; Lee, E.; Tan, J.; Yang, W.; Kim, B.; Moon, J. A New Class of Chiral Semiconductors: Chiral-Organic-Molecule-Incorporating Organic-Inorganic Hybrid Perovskites. *Mater. Horiz.* **2017**, *4*, 851.
(27) Göhler, B.; Hamelbeck, V.; Markus, T. Z.; Kettner, M.; Hanne, G. F.; Vager, Z.; Naaman, R.; Zacharias, H. Spin Selectivity in Electron Transmission through Self-Assembled Monolayers of Double-Stranded DNA. *Science* **2011**, *331*, 894−897.
(28) Sun, D.; Zhang, C.; Kavand, M.; van Schooten, K. J.; Malissa, H.; Groesbeck, M.; McLaughlin, R.; Boehme, C.; Vardeny, Z. V. Spintronics of Organometal Trihalide Perovskites. *arXiv (Materials Science)*, August 2, 2016, 1608.00993, ver. 1. https://arxiv.org/abs/1608.00993 (accessed 2016/08/02).
(29) Sun, D.; Zhang, C.; Kavand, M.; Wang, J.; Malissa, H.; Liu, H.; Popli, H.; Singh, J.; Vardeny, S. R.; Zhang, W.; Boehme, C.; Vardeny, Z. V. Surface-Enhanced Spin Current to Charge Current Conversion Efficiency in $CH_3NH_3PbBr_3$-Based Devices. *J. Chem. Phys.* **2019**, *151*, 174709.
(30) Yu, Z. G. Effective-Mass Model and Magneto-Optical Properties in Hybrid Perovskites. *Sci. Rep.* **2016**, *6*, 28576.
(31) Thouin, F.; Valverde-Chávez, D. A.; Quarti, C.; Cortecchia, D.; Bargigia, I.; Beljonne, D.; Petrozza, A.; Silva, C.; Srimath Kandada, A. R. Phonon Coherences Reveal the Polaronic Character of Excitons in Two-Dimensional Lead Halide Perovskites. *Nat. Mater.* **2019**, *18*, 349−356.
(32) Yin, J.; Li, H.; Cortecchia, D.; Soci, C.; Brédas, J.-L. Excitonic and Polaronic Properties of 2D Hybrid Organic-Inorganic Perovskites. *ACS Energy Lett.* **2017**, *2*, 417−423.
(33) Kresse, G.; Hafner, J. *Ab Initio* Molecular Dynamics for Liquid Metals. *Phys. Rev. B: Condens. Matter Mater. Phys.* **1993**, *47*, 558−561.
(34) Kresse, G.; Furthmuller, J. Efficient Iterative Schemes for *Ab Initio* Total-Energy Calculations Using a Plane-Wave Basis Set. *Phys. Rev. B: Condens. Matter Mater. Phys.* **1996**, *54*, 11169−11186.
(35) Perdew, J. P.; Burke, K.; Ernzerhof, M. Generalized Gradient Approximation Made Simple. *Phys. Rev. Lett.* **1997**, *78*, 1396−1396.
(36) Perdew, J. P.; Burke, K.; Ernzerhof, M. Generalized Gradient Approximation Made Simple. *Phys. Rev. Lett.* **1996**, *77*, 3865−3868.

https://dx.doi.org/10.1021/acsnano.0c04017
ACS Nano 2020, 14, 10370−10375